Generation of Solar UV and EUV Images from *SDO*/HMI Magnetograms by Deep Learning

Eunsu Park[1] , Yong-Jae Moon[1] , Jin-Yi Lee[2] , Rok-Soon Kim[3,4] , Harim Lee[2] , Daye Lim[1] , Gyungin Shin[1], and Taeyoung Kim[1,5]

[1] School of Space Research, Kyung Hee University, Yongin, 17104, Republic of Korea; moonyj@khu.ac.kr
[2] Department of Astronomy and Space Science, College of Applied Science, Kyung Hee University, Yongin, 17104, Republic of Korea
[3] Korea Astronomy and Space Science Institute, Daejeon, 34055, Republic of Korea
[4] University of Science and Technology, Daejeon, 34113, Republic of Korea
[5] InSpace Co., Ltd., Daejeon, 34111, Republic of Korea

Received 2019 June 8; revised 2019 September 11; accepted 2019 September 21; published 2019 October 11

Abstract

In this Letter, we apply deep-learning methods to the image-to-image translation from solar magnetograms to solar ultraviolet (UV) and extreme UV (EUV) images. For this, We consider two convolutional neural network models with different loss functions, one (Model A) is with L1 loss (L_1), and the other (Model B) is with L_1 and cGAN loss (L_{cGAN}). We train the models using pairs of *Solar Dynamics Observatory* (*SDO*)/Atmospheric Imaging Assembly (AIA) nine-passband (94, 131, 171, 193, 211, 304, 335, 1600, and 1700 Å) UV/EUV images and their corresponding *SDO*/Helioseismic and Magnetic Imager (HMI) line-of-sight (LOS) magnetograms from 2011 to 2016. We evaluate the models by comparing pairs of *SDO*/AIA images and the corresponding ones generated in 2017. Our main results from this study are as follows. First, the models successfully generate *SDO*/AIA-like solar UV and EUV images from *SDO*/HMI LOS magnetograms. Second, in view of three metrics (pixel-to-pixel correlation coefficient, relative error, and the percentage of pixels having errors less than 10%), the results from Model A are mostly comparable or slightly better than those from Model B. Third, in view of the rms contrast measure, the generated images by Model A are much more blurred than those by Model B because of L_{cGAN} specialized for generating realistic images.

Key words: methods: data analysis – Sun: atmosphere – techniques: image processing

1. Introduction

Over the past several decades, many astronomical observations have been made through multiwavelength observations. In the case of the Sun, several space missions, such as *Solar Heliospheric Observatory* (*SOHO*; Domingo et al. 1995), *Hinode* (Kosugi et al. 2007), *Solar Terrestrial Relations Observatory* (*STEREO*; Kaiser et al. 2008), and *Solar Dynamics Observatory* (*SDO*; Pesnell et al. 2012), have observed solar atmosphere, and they have captured various types of solar multiwavelength observations, such as ultraviolet (UV) images, extreme UV (EUV) images, and magnetograms. In particular, the UV and EUV observations by several instruments, including *SOHO*/Extreme-ultraviolet Imaging Telescope (EIT; Delaboudinière et al. 1995), Transition Region And Coronal Explorer (TRACE; Handy et al. 1999), *STEREO*/ Extreme UltraViolet Imager (EUVI; Howard et al. 2008), and *SDO*/Atmospheric Imaging Assembly (AIA; Lemen et al. 2012), have allowed us to identify several solar atmospheric structures such as coronal holes, filaments, coronal loops, and active regions. In addition, they have provided us with detailed measurements of plasma parameters such as electron densities and temperature (e.g., Del Zanna & Mason 2018). The magnetic field of the Sun, which is another important solar observational parameter, is the underlying cause of many diverse phenomena as a part of solar activity (Solanki et al. 2006; Wiegelmann et al. 2014). There have been several instruments for the measurements of solar photospheric magnetic fields such as *SOHO*/Michelson Doppler Imager (MDI; Scherrer et al. 1995) and *SDO*/Helioseismic and

Magnetic Imager (HMI; Scherrer et al. 2012; Schou et al. 2012).

The deep neural network (DNN; Lecun et al. 2015), which is called "Deep Learning," is a kind of artificial neural network, and is developed to learn the way humans think and recognize an object using their deep hierarchical layer structures. The DNN has become very popular and is applied to several fields due to a large amount of data (big data), advanced hardware, and improvements in machine-learning algorithms. The convolutional neural network (CNN; Lecun et al. 1998) is the most popular deep-learning method in the area of image processing and computer vision. In general, the CNN models consist of convolution filters, and the filters extract features from their data sets. The CNN models train the filters to select and extract features automatically without human intervention, while traditional machine-learning algorithms require researchers to manually select and construct feature extractors. Recently, the generative adversarial network (GAN; Goodfellow et al. 2014), which is one of the popular deep-learning methods, has been widely examined in several generations of tasks. In particular, Isola et al. (2016) suggested a general purposed solution based on a conditional generative adversarial network (cGAN; Mirza & Osindero 2014) and a deep convolutional generative adversarial network (DCGAN; Radford et al. 2015) to resolve the image-to-image translation problems. The model by Isola et al. (2016) very successfully works for various types of image-to-image translations: labels to the street scenes, label to facade, black and white image to color one, satellite view to map, day view to night view, and even sketch image to photo.

There have been a few attempts to translate between solar images using deep-learning methods. Galvez et al. (2019)

applied a deep-learning model based on CNNs to generate solar UV/EUV images using *SDO*/HMI vector magnetograms. Kim et al. (2019) suggested a deep-learning model based on cGAN to generate solar magnetograms using *SDO*/AIA images and then applied the model to *STEREO*/EUVI images to produce solar farside magnetograms.

In this Letter, we apply a deep-learning method to the image-to-image translation from solar magnetograms to solar UV and EUV images. For training the model, we use *SDO*/HMI and *SDO*/AIA all-passband data. Then we quantitatively evaluate the results of the model and discuss them in view of underlying physics. This Letter is organized as follows. The data will be described in Section 2, and the image-to-image translation method in Section 3. Results are given in Section 4, and a brief summary is presented in Section 5.

2. Data

SDO is a spacecraft mission that investigates how a solar magnetic field is generated and structured and how this stored magnetic energy is released into the heliosphere and geospace as solar wind, energetic particles, and variations in the solar irradiance with three instruments (Pesnell et al. 2012). HMI is an instrument of the *SDO*, which is designed to measure the Doppler shift, intensity, and vector magnetic field at the solar photosphere (Scherrer et al. 2012; Schou et al. 2012). AIA, which is another instrument of the *SDO*, is designed to provide multiple simultaneous images with views of the entire solar corona and transition region (Lemen et al. 2012). We use pairs of *SDO*/HMI line-of-sight (LOS) magnetograms and *SDO*/AIA nine-passband UV and EUV images. We select pairs of full-disk *SDO*/HMI magnetograms and *SDO*/AIA images with 6 hr cadence (four pairs per day) from 2011 to 2017 for nine passbands (94, 131, 171, 193, 211, 304, 335, 1600, and 1700 Å). We first make level 1.5 images by calibrating, rotating, and centering the images. We divide all AIA images by exposure time to make all AIA images have a homogeneous exposure condition (DN s^{-1}). To compensate for the instrument degradation over time for seven AIA EUV passbands (Boerner et al. 2014), we find a degrading factor for each passband and date using a SolarSoft routine (aia_get_response.pro) with a reference date of 2011 January 1. Then, we apply each factor to the corresponding image. Also, we coalign the AIA and HMI images by fixing the solar disk size, and downsample the images to 1024 by 1024 for computational capability. We use an AIA image with the range of 0 DN s^{-1} for minimum and $2^{14} - 1$ DN s^{-1} for maximum. To input the AIA data to our models, we convert the data to the log scale (0–14), then re-scale to (−1 to 1). Detail data pipeline code is available at our GitHub repository.[6] We exclude images with poor quality, including too noisy images due to solar flares, incorrect header information, and untypical images for reasons such as the transit of a planet. As a result, we make a total of 9985 pairs of *SDO*/HMI magnetograms and *SDO*/AIA images for each passband (total of 99,850 images). We separate our data sets into training, validation, and test in chronological order. We select 714 pairs for each passband from 2017 January to 2017 June for the validation data set, 727 pairs from 2017 July to 2017 December for the test data set, and the remaining 8544 pairs for the training data set.

3. Method

We consider two CNN models, one is Model A with L1 loss (L_1), and the other is Model B with L_1 and cGAN loss (L_{cGAN}). Details about functions of the two losses are described in Appendix A. The two models have a generative network, called "generator." The generator has an objective, which is to generate *SDO*/AIA-like images using *SDO*/HMI magnetograms. The generators of the two models have the same structure, but we train them with different losses.

In the case of Model A, we train its generator by minimizing L_1 to satisfy the objective of the generator. To minimize the loss, we use the adaptive momentum estimation solver (ADAM; Kingma & Ba 2014) as an optimizer for the generator; detailed hyperparameters are described in Appendix C. The training process of Model A is described in Appendix B.1

In the case of Model B, we use both L_1 and L_{cGAN}. To apply L_{cGAN}, this model includes a discriminative network, called "discriminator." More details about the architectures of the two networks and codes are available at https://github.com/eunsu-park/solar_euv_generation. Figure 1 shows the main structure of Model B. The discriminator has an objective, which is to distinguish pairs of *SDO*/AIA images and *SDO*/HMI magnetograms, as denoted "Real pair," from pairs of generated images and *SDO*/HMI magnetograms, as denoted "Fake pair." This process is based on a competition between the generator and the discriminator in that they have adversarial objectives to each other. We expect L_1 contributes to minimizing the difference between *SDO*/AIA images and generated ones, and L_{cGAN} contributes to generating realistic *SDO*/AIA-like images. To minimize or maximize the losses, we use the ADAM optimizer, the same as Model A, for the generator and the discriminator. The training process of Model B is described in Appendix B.2
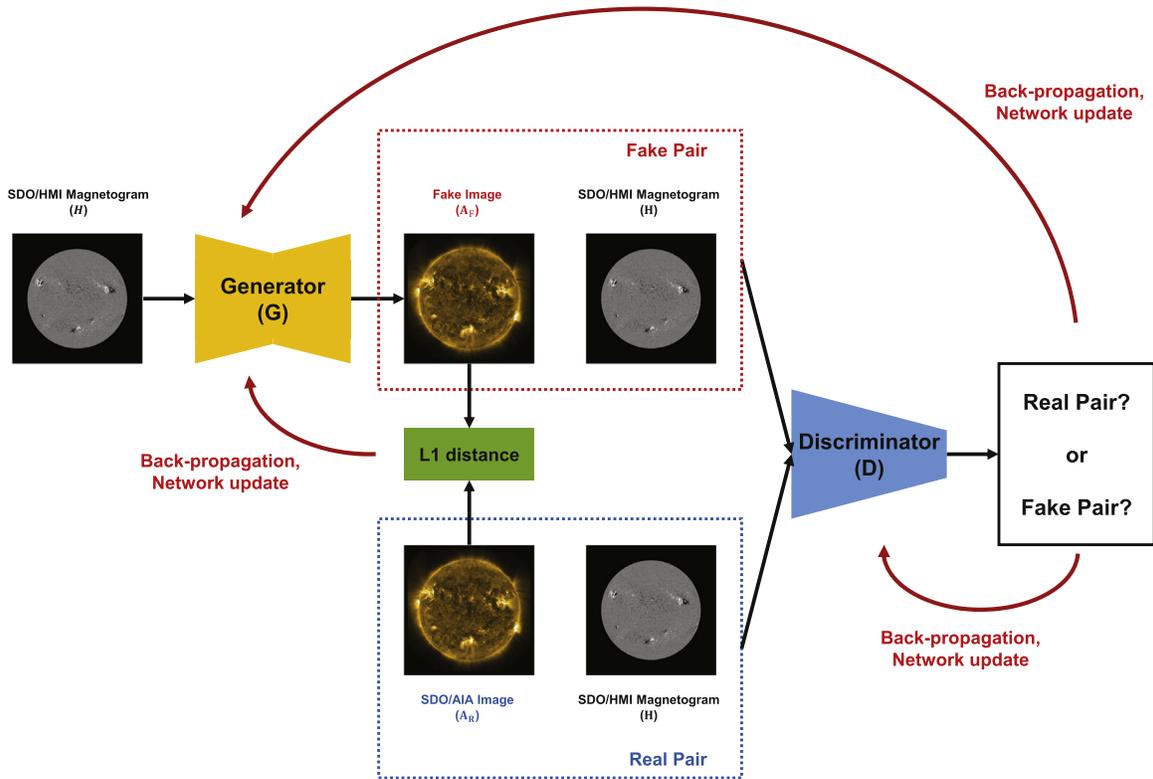
We train the models with 500,000 iterations, and we save the generators every 10,000 iterations. As a result, we acquire 50 generators while the generators (and the discriminator) are trained for 500,000 iterations (∼59 epochs). Here one iteration is when one pair of images is trained in our model, and one epoch is when an entire training data set of 8544 pairs is done in our model. In the validation step, we compare the *SDO*/AIA images with the generated images by the 50 generators using the validation data set, then we select the best model among the 50 saved generators. In the test step, we estimate the model performances of selected generator networks in the validation step. We repeat the training, validation, and test steps nine times for each passband, so we acquire a total of 450 generators and the 9 best generators for each passband.

4. Results and Discussion

To test our results, we calculate three types of metrics between *SDO*/AIA images and the generated ones for the entire test data sets. The first metric is the pixel-to-pixel correlation coefficient (CC; higher is better). We can get high CC when our model generates well not only pixel values but also locations of brightening. The second metric is relative error (RE; closer to 0 is better) of total pixel value (Φ_i), which is given by

$$\mathrm{RE}_i = (\Phi_i^{\text{generated}} - \Phi_i^{\text{AIA}})/\Phi_i^{\text{AIA}}, \qquad (1)$$

Figure 1. A flowchart and structures of Model B. G is the generator network, D is the discriminator network, H is an SDO/HMI magnetogram, A_R is an SDO/AIA image, and A_F is a Fake image by the generator. The blue box is a Real pair (H, A_R), and the red box is a Fake pair (H, A_F).

where i is a serial number of 727 test samples. The third metric is the percentage of pixels having errors less than 10% (PPE10; higher is better). For three metrics, we perform 4×4 binning of output images to make ones that are 256 by 256, and we consider pixels on the solar disk. In addition to the metrics, we calculate the rms contract measure (CM; higher is more clear) to measure the blurriness of the generated images, which is given by

$$\mathrm{CM}_i = \sqrt{\frac{1}{N}\sum(I_j - \bar{I})^2}, \qquad (2)$$

where i is a serial number of 727 test samples, j is a pixel number, I_j is a pixel value of the jth pixel, and $\bar{I}$ is the average pixel values on the solar disk.

Table 1 shows the average CC, RE, PPE10, and CM values of the entire test data sets for each passband. For the three metrics and CM in Table 1, we unlog the output data and compare in the linear scale with the range of (0 DN s^{-1}–$2^{14} - 1$ DN s^{-1}) as described in Section 2. CC values of Model A and Model B are higher than 0.69 and 0.66, and the average CC values of the two models are 0.84 and 0.83, respectively. The absolute values of RE of Model A and Model B are less than 0.18 and 0.17, and the average RE values of the two models are 0.07 and 0.06, respectively. PPE10 values of Model A range from 24.6% to 96.6% with an average value of 46.2%, and those of Model B range from 21.8% to 92.7% with an average value of of 43.5%. The percentage of pixels having errors less than 50% of values of Model A range from 80.9% to 99.9% with an average value of 93.4%, and those of Model B range from 77.2% to 99.9% with an average value of 92.1%. In view of these three metrics, the results from Model A are

mostly comparable or slightly better than those from Model B for most passbands. However, Model B has better CM values than Model A, which means that the results from Model A are more blurred than those from Model B. Figure 2 shows a comparison between real SDO/AIA images and the generated ones from the two models for a data set (nine passbands) at 18:00 UT on 2017 July 11. It was already noted that the results from the image translation models using L_{cGAN} could be more realistic than those from the models using only L_1, because that L_1 only contributes to minimizing the difference between the generated images and the target images, but L_{cGAN} also contributes to generating realistic images (Isola et al. 2016; Ledig et al. 2016).

SDO/AIA observes the specific types of solar features depending on the passbands, which represent the characteristic temperatures of the primary ions for each passband (Lemen et al. 2012; see Table 1). Now we discuss our results according to the three groups classified by the temperature responses of the passbands with the results from Model B.
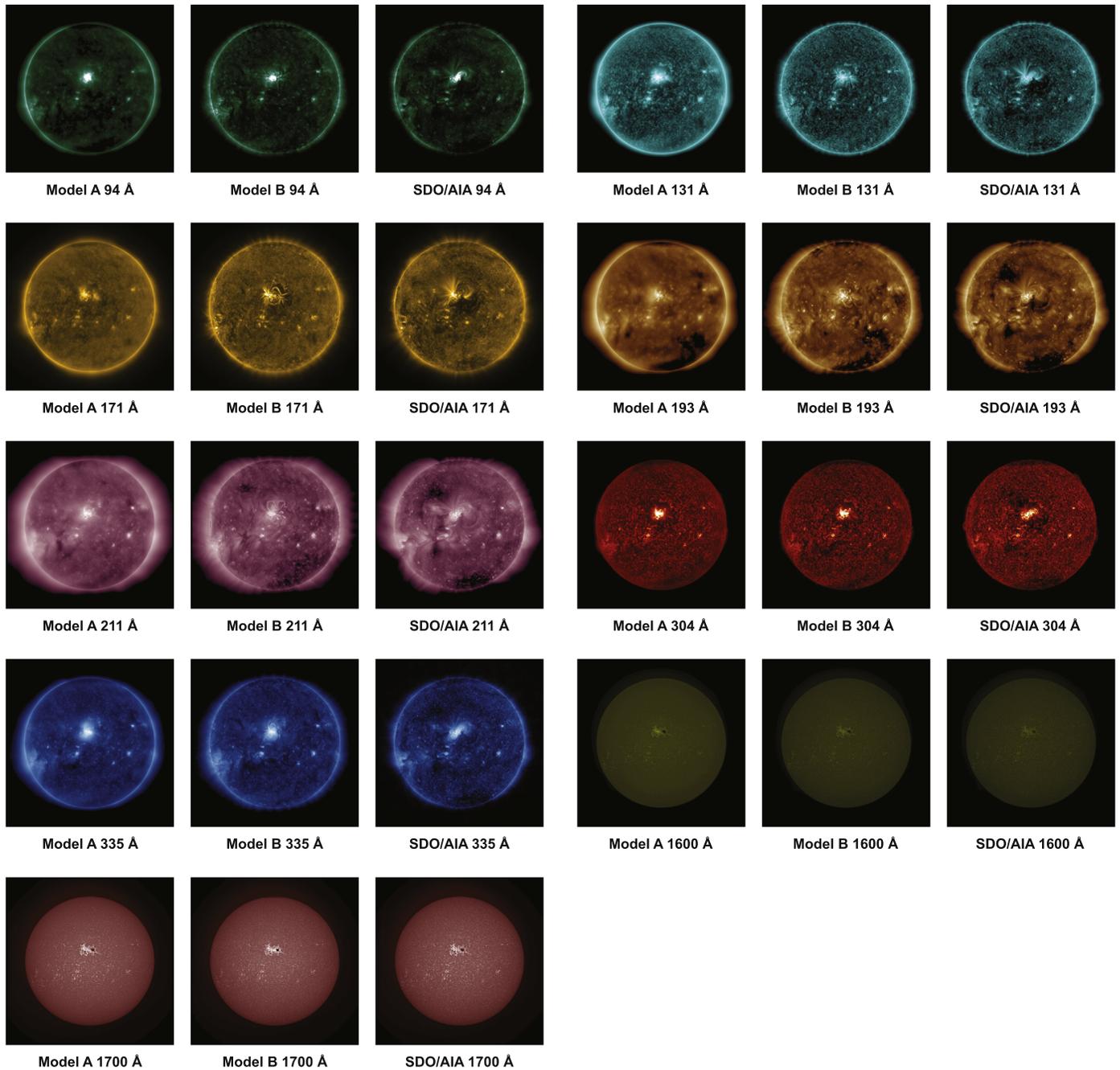
The first group corresponds to photospheric UV passbands, which are 1600 and 1700 Å. This group has CC values larger than 0.92 and absolute values of RE smaller than 0.11. In particular, the average correlation of 1700 Å is 0.95 (see Table 1), which is the best among all passbands. Galvez et al. (2019) also find that the 1600 and 1700 Å observations are easier to predict than other passbands. Figure 3 shows a comparison between generated 1600 and 1700 Å images and their corresponding AIA ones at 12:00 UT on 2017 August 7. As shown in the figure, the generated one is quite consistent with the real one, even the small-scale structures. This group has a high CC value (0.44 for 1700 Å and 0.46 for 1600 Å) with the corresponding SDO/HMI magnetograms compared to

Table 1
The Average Pixel-to-pixel Correlation Coefficient (CC), Relative Error (RE), the Percentage of Pixels Having Errors Less than 10% (PPE10), and Root Mean Square Contrast Measure (CM) for Each Passband

Passband (Å)	Temperature (K)	Region (Lemen et al. 2012)	Remark	Step	CC		RE		PPE10		CM	
					Model A	Model B	Model A	Model B	Model A	Model B	Model A	Model B
1700	4500	temperature minimum, photosphere	Group 1	validation	0.97	0.95	−0.01	0.01	98.2	93.8	193.18	208.91
				test	0.97	0.95	0.01	0.02	96.6	92.7	197.44	209.87
1600	10,000	transition region, upper photosphere		validation	0.94	0.92	0.04	0.06	81.0	73.3	6.75	8.57
				test	0.94	0.92	0.11	0.11	52.3	50.4	6.88	9.23
304	50,000	chromosphere, transition region	Group 2	validation	0.86	0.84	−0.06	−0.05	37.1	35.2	16.47	20.38
				test	0.84	0.83	−0.18	−0.17	25.5	25.3	15.96	19.75
171	600,000	quiet corona, upper transition region		validation	0.72	0.68	−0.06	−0.04	28.0	25.7	69.46	86.13
				test	0.69	0.66	−0.05	−0.04	27.3	25.3	66.26	80.73
193	1000,000	corona, hot flare plasma	Group 3	validation	0.82	0.78	0.05	0.06	25.8	23.9	100.28	106.14
				test	0.78	0.74	0.07	0.07	24.6	23.3	95.54	102.50
211	2000,000	active region corona		validation	0.88	0.81	0.07	0.07	25.7	22.5	43.49	44.77
				test	0.86	0.78	0.08	0.08	25.2	21.8	40.45	43.02
335	2500,000	active region corona		validation	0.89	0.88	−0.03	0.04	49.3	46.1	2.57	3.30
				test	0.86	0.85	−0.03	0.04	49.2	46.3	2.47	3.10
94	6000,000	flaring corona		validation	0.83	0.79	−0.02	−0.02	71.5	67.2	0.61	0.70
				test	0.79	0.75	−0.03	−0.02	72.0	67.4	0.60	0.72
131	10,000,000	transition region, flaring corona		validation	0.84	0.81	−0.04	−0.02	43.7	40.0	2.94	3.42
				test	0.81	0.78	−0.04	−0.03	42.9	39.4	2.77	3.29
		Test Average			0.84	0.83	0.07	0.06	46.2	43.5	47.60	52.47

4
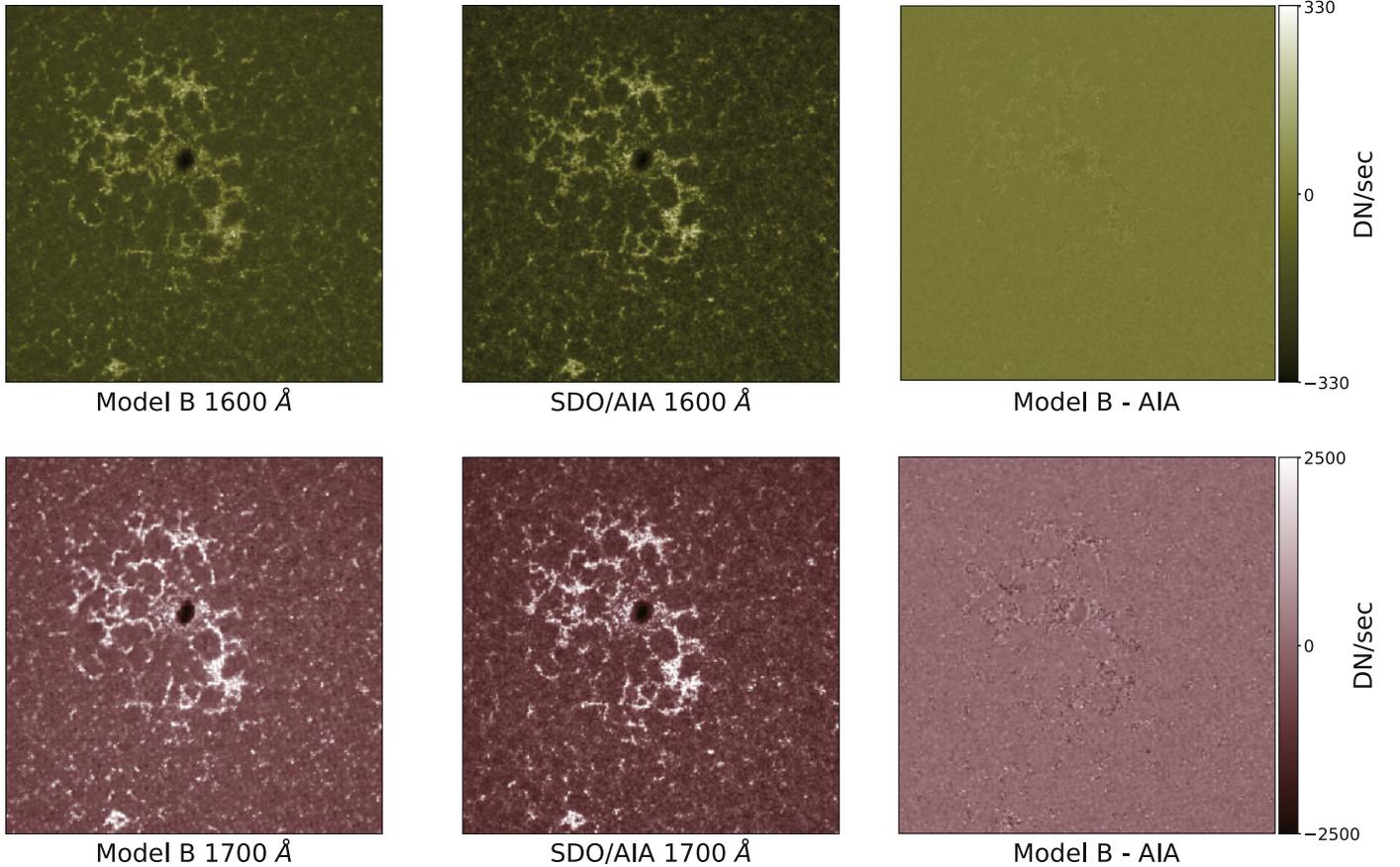
2017 July 11 18:00 UT

Figure 2. Comparison between real *SDO*/AIA images and the generated ones for a data set (nine passbands) at 12:00 UT on 2017 July 11. The first column represents generated images by Model A, the second column represents generated images by Model B, and the third column represents *SDO*/AIA images.

other passbands (average value of 0.36). This pronounced similarity between brightness in 1600 Å and the underlying photospheric magnetic field is reported by Loukitcheva et al. (2009) and Barczynski et al. (2018). These results imply that these similar structures have caused the high CC and RE scores.

The second group corresponds to chromospheric, transition region, and quiet coronal EUV passbands, which are 171 and 304 Å. Figure 4 shows a comparison between generated 171 and 304 Å images and their corresponding AIA ones at 12:00 UT on 2017 August 11. As shown in the 171 Å images, the

morphology of generated loops does not well match that of the AIA ones. These detailed structures observed with high resolution are not clearly observed in other passbands, which means that our model suffers from greater difficulty in generating in local structures than in global structures. In the case of 304 Å images, the average CC value is 0.83 with −0.17 RE, which is not so good compared to that of group 1. The reason may be due to complex chromospheric structures such as filaments and the instrument degradation of this passband. In fact, it is well known that the instrument degradation over time for the 304 Å EUV passband is the largest among all passbands

2017 August 7 12:00 UT

Figure 3. Comparison between generated 1600 and 1700 Å images by Model B and *SDO*/AIA ones at 12:00 UT on 2017 August 7. The first column represents generated images by Model B, the second column represents *SDO*/AIA ones, and the last column represents the difference maps between generated images and *SDO*/AIA ones.

(Boerner et al. 2014). Even though we have made a correction using the degrading factor, there is a possibility that the instrument degradation effects still have remained.

The last group corresponds to active region coronal and flaring coronal EUV passbands, which are all the remaining ones as shown in Table 1. This group has CC values greater than 0.74 and absolute values of RE less than 0.08. These results seem to be related to the fact that strong magnetic fields in HMI magnetograms are mostly located in solar active regions, and EUV brightenings are mostly found in active regions and flaring sites. We understand that our model learns well the relationship between magnetic fields and EUV brightness. Our results are also supported by that the EUV brightenings are due to the heating by small-scale magnetic field reconnections such as nanoflare heating and/or by MHD waves (Parker 1972; Sturrock & Uchida 1981; Parker 1983; van Ballegooijen 1986; Heyvaerts & Priest 1992).
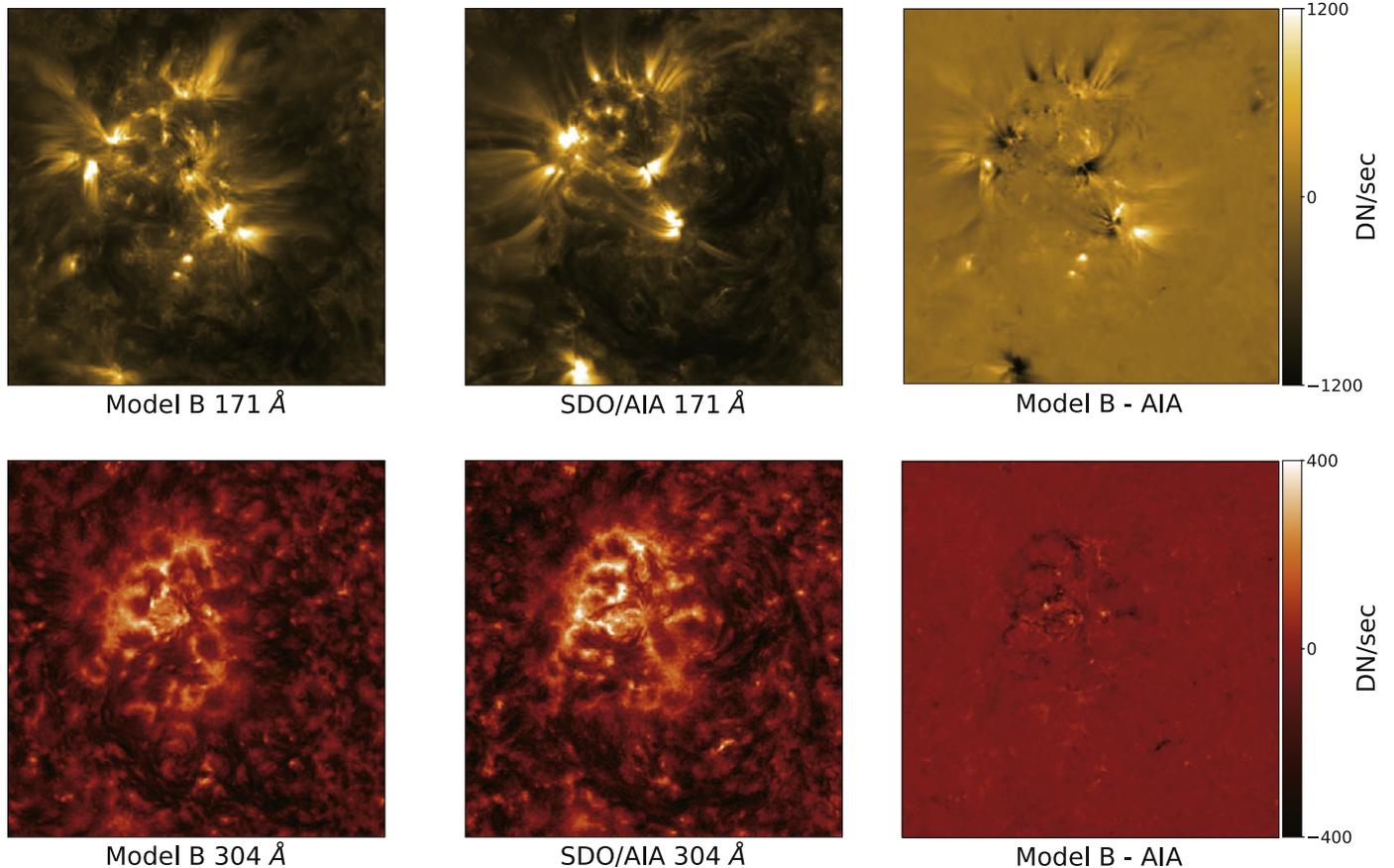
5. Conclusion and Summary

In this Letter, we have applied a deep-learning method to the image-to-image translation from solar magnetograms to solar UV and EUV images. We have trained two CNN models, one is with L_1, and the other is with L_1 and L_{cGAN}. We selected 9985 pairs of the nine-passband *SDO*/AIA UV and EUV images and the corresponding *SDO*/HMI magnetograms. We separated our data sets into training, validation, and test sets in

chronological order. We trained our models using 8544 pairs from 2011 January to 2016 December, validated our models using 714 pairs from 2017 January to 2017 June, and tested our models using 727 pairs from 2017 July to 2017 December.

The main results of this study are as follows. First, the models successfully generated *SDO*/AIA-like solar UV and EUV images from *SDO*/HMI magnetograms. Second, CC values from Model A range from 0.69 to 0.97, and those from Model B range from 0.66 to 0.95. Third, RE values from Model A and Model B are within −0.18 and −0.17, respectively. Fourth, 46.2% and 43.5% of pixels of the generated images from Model A and Model B have a pixel value error within 10%, respectively. Fifth, in view of the three metrics (CC, RE, and PPE10), the results from Model A are mostly comparable or slightly better than those from Model B. Sixth, in view of CM, the generated images by Model A are much more blurred than those by Model B because of L_{cGAN} being specialized for generating realistic images. Then we have briefly discussed our results in view of the physical connection between photospheric magnetic fields and the formation of UV/EUV passbands. Further detailed discussions are beyond the scope of this Letter and remain as open questions.

In this study we have trained, validated, and tested the models using chronologically separated data sets. This approach is suitable in view of the space weather operator (Nishizuka et al. 2017; Park et al. 2018), but the results from this approach could not fully consider the solar cycle phase

2017 August 7 12:00 UT

Figure 4. Comparison between generated 171 and 304 Å images by Model B and *SDO*/AIA ones at 12:00 UT on 2017 August 7. The first column represents generated images by Model B, the second column represents *SDO*/AIA ones, and the last column represents the difference maps between generated images and *SDO*/AIA ones.

effect and the time-varied AIA degradation effects. Thus, there is a possibility that the results may be improved if we use other data sets such as randomly or nonchronologically separated sets.

Recently, UV/EUV observations have become more important in space weather. For example, coronal holes, which are observed from the UV/EUV observations, have become a major cause of space weather disturbances, while solar activities are very quiet. However, due to the absorption by the Earth's atmosphere, these observations have been possible since the late 1990s, the so-called *SOHO* era. Before the *SOHO* era, there were several observational blanks such as the "EUV Hole" (Tobiska et al. 2000) because of the limitations of EUV as seen through satellite observations. On the other hand, the magnetic field of the Sun has been continuously observed at various ground stations using vector magnetograms since the 1970s (Livingston et al. 1976; Jones et al. 1992). If we can generate EUV images from the magnetograms, we can extend our study on solar activity and space weather effects using more extended data sets.

Our results could be improved by considering other data sets such as vector magnetic fields to complement the morphology of generated structures. Also, we are trying to improve the results by developing other models such as image translation models for high-resolution images to generate small-scale structures. In the future, video translation models would be more promising by considering temporal and spatial evolution together. Our results have demonstrated a sufficient possibility that this methodology can be applied to many scientific fields that use several multiwavelength images, in not only astronomy but also other scientific fields.

Appendix A
Loss function

The function of L_{cGAN} is described as follows:

$$L_{cGAN}(G, D) = E_{x,y}[\log D(x, y)]$$
$$+ E_x[\log(1 - D(x, G(x)))], \quad (3)$$

where G is the generator, D is the discriminator, x, y, and $G(x)$ are the real input, real output, and fake output, respectively. $D(x, y)$ is the probability calculated by the discriminator using Real pair, and $D(x, G(x))$ is the probability calculated by the discriminator using Fake pair. G tries to minimize the L_{cGAN} loss function against an adversarial D that tries to maximize the L_{cGAN} loss function. The function of L_1 is described as follows:

$$L_1 = E_{x,y}(\|y - G(x)\|). \quad (4)$$

G tries to minimize this the L_1 loss. The final loss function for this work can be found with G^* given by

$$G^* = \operatorname{argmin}_G \max_D L_{cGAN}(G, D) + \lambda L_1(G), \quad (5)$$

where λ is the relative weight of L_{cGAN} loss and L_1 loss. In this work, we used 100 for the relative weight like Isola et al. (2016).

Appendix B
Training Process

B.1. Model A

We train Model A as follows:

1. We prepare an SDO/AIA image and a corresponding SDO/HMI magnetogram.
2. The generator generates an SDO/AIA-like image from the SDO/HMI magnetogram.
3. The model calculates L_1 between the SDO/AIA image and the generated one, then back-propagates the value of L_1 to the generator.
4. The generator updates itself by minimizing L_1 to generate more realistic images.
5. We iterate the above steps.

B.2. Model B

We train Model B as follows:

1. We prepare an SDO/AIA image and a corresponding SDO/HMI magnetogram.
2. The generator generates an SDO/AIA-like image from the SDO/HMI magnetogram.
3. The model calculates L_1 between the SDO/AIA image and the generated one, then back-propagates the value of L_1 to the generator.
4. The discriminator distinguishes the Real pair from the Fake pair, then returns the result as a percentage value (0 for Fake pair, 1 for Real pair).
5. The model calculates L_{cGAN} using the result, then back-propagates L_{cGAN} to the generator and the discriminator.

6. The generator updates itself by minimizing both L_{cGAN} and L_1 to generate more realistic images.
7. The discriminator updates itself by maximizing L_{cGAN} to distinguish well both the Real pair and Fake pair.
8. We iterate the above steps.

Appendix C
Hyperparameter

The initializer for the Convolution layers and the Convolution-Transpose layers is a normal distribution with 0.0 mean and 0.02 standard deviation. The initializer for the Batch-Normalization layers is a normal distribution with 1.0 mean and 0.02 standard deviation. We use the ADAM solver as the optimizer with a learning rate of 2×10^{-4}, momentum $\beta 1$ of 0.5, and momentum $\beta 2$ of 0.999.

ORCID iDs

Eunsu Park ⓘ https://orcid.org/0000-0003-0969-286X
Yong-Jae Moon ⓘ https://orcid.org/0000-0001-6216-6944
Jin-Yi Lee ⓘ https://orcid.org/0000-0001-6412-5556
Rok-Soon Kim ⓘ https://orcid.org/0000-0002-9012-399X
Harim Lee ⓘ https://orcid.org/0000-0002-9300-8073
Daye Lim ⓘ https://orcid.org/0000-0001-9914-9080

References

Barczynski, K., Peter, H., Chitta, L. P., et al. 2018, A&A, 619, A5
Boerner, P. F., Testa, P., Warren, H., et al. 2014, SoPh, 289, 2377
Del Zanna, G., & Mason, H. E. 2018, LRSP, 15, 5
Delaboudinière, J.-P., Artzner, G. E., Brunaud, J., et al. 1995, SoPh, 162, 291
Domingo, V., Fleck, B., & Poland, A. I. 1995, SoPh, 162, 1
Galvez, R., Fouhey, D. F., Jin, M., et al. 2019, ApJS, 242, 7
Goodfellow, I. J., Pouget-Abadie, J., Mirza, M., et al. 2014, arXiv:1406.2661
Handy, B. N., Acton, L. W., Kankelborg, C. C., et al. 1999, SoPh, 187, 229
Heyvaerts, J., & Priest, E. R. 1992, ApJ, 390, 297
Howard, R. A., Moses, J. D., Vourlidas, A., et al. 2008, SSRv, 136, 67
Isola, P., Zhu, J.-Y., Zhou, T., et al. 2016, arXiv:1611.07004
Jones, H. P., Duvall, T. L., Harvey, J. W., et al. 1992, SoPh, 139, 211
Kaiser, M. L., Kucera, T. A., Davila, J. M., et al. 2008, SSRv, 136, 5
Kim, T., Park, E., Lee, H., et al. 2019, NatAs, 3, 397
Kingma, D. P., & Ba, J. 2014, arXiv:1412.6980
Kosugi, T., Matsuzaki, K., Sakao, T., et al. 2007, SoPh, 243, 3
Lecun, Y., Bengio, Y., & Hinton, G. 2015, Natur, 521, 436
Lecun, Y., Bottou, L., Bengio, Y., & Haffner, P. 1998, Proc. IEEE, 86, 2278
Ledig, C., Theis, L., Huszar, F., et al. 2016, arXiv:1609.04802
Lemen, J. R., Title, A. M., Akin, D. J., et al. 2012, SoPh, 275, 17
Livingston, W. C., Harvey, J., Pierce, A. K., et al. 1976, ApOpt, 15, 33
Loukitcheva, M., Solanki, S. K., & White, S. M. 2009, A&A, 497, 273
Mirza, M., & Osindero, S. 2014, arXiv:1411.1784
Nishizuka, N., Sugiura, K., Kubo, Y., et al. 2017, ApJ, 835, 156
Park, E., Moon, Y.-J., Shin, S., et al. 2018, ApJ, 869, 91
Parker, E. N. 1972, ApJ, 174, 499
Parker, E. N. 1983, ApJ, 264, 642
Pesnell, W. D., Thompson, B. J., & Chamberlin, P. C. 2012, SoPh, 275, 3
Radford, A., Metz, L., & Chintala, S. 2015, arXiv:1511.06434
Scherrer, P. H., Bogart, R. S., Bush, R. I., et al. 1995, SoPh, 162, 129
Scherrer, P. H., Schou, J., Bush, R. I., et al. 2012, SoPh, 275, 207
Schou, J., Scherrer, P. H., Bush, R. I., et al. 2012, SoPh, 275, 229
Solanki, S. K., Inhester, B., & Schüssler, M. 2006, RPPh, 69, 563
Sturrock, P. A., & Uchida, Y. 1981, ApJ, 246, 331
Tobiska, W. K., Woods, T., Eparvier, F., et al. 2000, JASTP, 62, 1233
van Ballegooijen, A. A. 1986, ApJ, 311, 1001
Wiegelmann, T., Thalmann, J. K., & Solanki, S. K. 2014, A&ARv, 22, 78